

Characteristics of the leading Lyapunov vector in a turbulent channel flow

Nikolay Nikitin[†]

Institute of Mechanics, Lomonosov Moscow State University, 1 Michurinsky prospect,
119899 Moscow, Russia

(Received 14 March 2017; revised 26 March 2018; accepted 17 May 2018;
first published online 26 June 2018)

The values of the highest Lyapunov exponent (HLE) λ_1 for turbulent flow in a plane channel at Reynolds numbers up to $Re_\tau = 586$ are determined. The instantaneous and statistical properties of the corresponding leading Lyapunov vector (LLV) are investigated. The LLV is calculated by numerical solution of the Navier–Stokes equations linearized about the non-stationary base solution corresponding to the developed turbulent flow. The base turbulent flow is calculated in parallel with the calculation of the evolution of the perturbations. For arbitrary initial conditions, the regime of exponential growth $\sim \exp(\lambda_1 t)$ which corresponds to the approaching of the perturbation to the LLV is achieved already at $t^+ < 50$. It is found that the HLE increases with increasing Reynolds number from $\lambda_1^+ \approx 0.021$ at $Re_\tau = 180$ to $\lambda_1^+ \approx 0.026$ at $Re_\tau = 586$. The LLV structures are concentrated mainly in a region of the buffer layer and are manifested in the form of spots of increased fluctuation intensity localized both in time and space. The root-mean-square (r.m.s.) profiles of the velocity and vorticity intensities in the LLV are qualitatively close to the corresponding profiles in the base flow with artificially removed near-wall streaks. The difference is the larger concentration of LLV perturbations in the vicinity of the buffer layer and a relatively larger (by approximately 80 %) amplitude of the vorticity pulsations. Based on the energy spectra of velocity and vorticity pulsations, the integral spatial scales of the LLV structures are determined. It is found that LLV structures are on average twice narrower and twice shorter than the corresponding structures of the base flow. The contribution of each of the terms entering into the expression for the production of the perturbation kinetic energy is determined. It is shown that the process of perturbation development is essentially dictated by the inhomogeneity of the base flow, as well as by the presence of transversal motion in it. Neglecting of these factors leads to a significant underestimation of the perturbation growth rate. The presence of near-wall streaks in the base flow, on the contrary, does not play a significant role in the development of the LLV perturbations. Artificial removal of streaks from the base flow does not change the character of the perturbation growth.

Key words: turbulence simulation, turbulent boundary layers

[†] Email address for correspondence: nvnikitin@mail.ru

1. Introduction

The behaviour of spatio-temporal chaotic systems remains difficult to explain and predict, despite the considerable efforts spent on their study. Turbulent flows are among such difficult predictable systems. Even the simplest statistical correlations, which have been extensively studied experimentally, such as the law of resistance in a circular pipe, do not yet have a theoretical explanation. The question remains to what extent the chaotic behaviour of the system in time is associated with spatial disorder and whether knowledge of the spatial structure is sufficient for predicting temporal dynamics. The degree of predictability of the space–time system is associated with the characteristics of its stability: how quickly the spatial structure changes under the influence of small random disturbances.

The development of small-scale perturbations in the near-wall turbulent flows is usually associated with the presence of near-wall streaky structures. Streaky structures are a typical attribute of the near-wall shear flows. They are observed both in natural and in controlled conditions, in laboratory experiments and in numerical simulations. The streaks occur in the boundary layers at the stage of transition from laminar flow to turbulent (Klebanoff, Tidstrom & Sargent 1962) and retain in the developed turbulent flows (Kline *et al.* 1967). Large-scale streaks in the longitudinal velocity are explained by the presence of longitudinal vortices and occur under the action of the so-called ‘lift-up’ effect (Landahl 1980). In transitional boundary layers longitudinal vortices are selected from random disturbances of the incoming flow. Small-scale vortices rapidly decay without a noticeable effect on the main flow, while long-wave vortices, during their decay downstream, make appreciable distortions in the distribution of the longitudinal velocity. The growth of streaky structures in the laminar boundary layer occurs in spite of the linear stability of the flow. Nevertheless, this process is satisfactorily described by the linearized equations due to non-normality of the corresponding linear operator, which allows transient (non-modal) growth of disturbances preceding their final exponential decay. Optimal perturbations which grow more than other perturbations have the form of elongated streaky structures with characteristics that resemble experimental ones (Butler & Farrell 1992; Reddy & Henningson 1993; Trefethen *et al.* 1993; Westin *et al.* 1994; Matsubara & Alfredsson 2001; Schmid & Henningson 2001). Distortion of the boundary layer by the free-stream vortical disturbances can provoke secondary instability and transition to turbulence, bypassing the stage of Tollmien–Schlichting wave development. Recent reviews of bypass transition studies are given in Durbin & Wu (2007), Zaki (2013).

In developed (post-transitional) near-wall turbulent flows, streaky structures remain, but become rapidly changing both in space and in time (Kline *et al.* 1967). For the most part they are concentrated in the buffer layer. Their mean streamwise extent is approximately 10^3 and mean spanwise separation is approximately 10^2 wall units (Smith & Metzler 1983). According to the generally accepted point of view streaky structures are involved in the process of maintaining near-wall turbulence (Kim, Kline & Reynolds 1971; Hamilton, Kim & Waleffe 1995; Jiménez & Pinelli 1999; Waleffe 1995, 1997; Schoppa & Hussain 2002). A variety of models have been proposed to justify the recurring appearance of streaky structures in near-wall turbulent flows and, in particular, to explain the universal linear dimensions of these structures (Jang, Benney & Gran 1986; Sreenivasan 1988; Brooke & Hanratty 1993; Butler & Farrell 1993; Waleffe, Kim & Hamilton 1993; Nikitin & Chernyshenko 1997; Schoppa & Hussain 1998; Waleffe 2003; Chernyshenko & Baig 2005; Del Álamo & Jiménez 2006; Farano *et al.* 2017).

The instability of near-wall streaks in turbulent flows has been investigated since the first visualization study by Kline *et al.* (1967). In this work (see also Kim *et al.* 1971), it was assumed that the main cause of the oscillations and subsequent destruction of streaks can be an instability of the Kelvin–Helmholtz type, developing in the regions of low-velocity streaks, where the local velocity profile $U(y)$ can have an inflection point. Swearingen & Blackwelder (1987) related streaky flows in a turbulent boundary layer to the more intensive streaks created by Görtler vortices on a concave surface. They found an inflectional instability of the $U(z)$ velocity distribution in shear layers separating high- and low-velocity streaks. A large number of studies have addressed the instability of a two-dimensional velocity distribution $U(y, z)$ in which spanwise-periodic or localized streaks are superimposed on a one-dimensional velocity profile (Waleffe 1997; Waleffe & Kim 1997; Schoppa & Hussain 1997, 1998; Kawahara *et al.* 1998). Two types of instability, varicose and sinuous, have been detected. Sinuous instability was found to be dominant in comparison to the varicose one. It arises at lower values of streak amplitude; the corresponding perturbation growth factors are larger than they are in varicose instability. Moreover, Schoppa & Hussain (1997) concluded that at typical streak amplitude in turbulent flows varicose instability rarely occurs. As for the sinuous instability, they speculated that even if it does occur, the related growth factors are restricted by a relatively minor value because of the viscous diffusion of streaks. Later (2002) these authors suggested that non-modal instability could be an alternative mechanism of perturbation growth in a streaky flow.

In most theoretical studies, streaks are assumed to be straight and steady whereas in real turbulent flows they are actually non-straight and non-steady. In addition, they are of finite streamwise extent, have an irregular spanwise distribution and have a variable amplitude in space and in time. Each of these factors can be important in assessment their stability. It is shown in Farrell & Ioannou (1996) that time dependency plays a central role in determining the instability of non-normal linear systems. In particular, time-dependent non-normality is capable of producing asymptotic instability. Farrell & Ioannou (2012) later concluded that the unsteadiness of streaks in turbulent flows is the determining factor for establishing self-maintenance of turbulence (see also Farrell *et al.* 2016). It should be noted that Farrell & Ioannou (2012) considered a model formulation in which the non-stationary streaky motion was assumed to be homogeneous in the streamwise direction. In the present work we show that flow variability in the streamwise direction is also a significant factor in assessing instability.

In the study of stability of systems with chaotic behaviour, classical definitions lose their meaning and have to be replaced by the concept of orbital stability, characterized by Lyapunov exponents and corresponding Lyapunov vectors. Lyapunov exponents and vectors characterize the stability of chaotic attractors in the same way as the eigenvalues and vectors characterize the stability of stationary solutions. The description of turbulent fluid flows from the standpoint of the behaviour of chaotic dynamic systems is not common today. This direction of research was developed most extensively in application to the problems of Rayleigh–Bénard turbulent convection (Egolf *et al.* 2000; Jayaraman *et al.* 2006; Xu & Paul 2016). In the present paper, the stability properties of developed turbulent flow in a plane channel are numerically studied. To date, there are several algorithms for calculating Lyapunov exponents and vectors (Parker & Chua 1989; Ginelli *et al.* 2007). First calculation of Lyapunov spectrum in a turbulent channel flow at a very low Reynolds number of $Re_\tau = 80$ with a restricted spatial resolution was made by Keefe, Moin & Kim (1992). Calculation of a Lyapunov spectrum with the corresponding vectors is a fairly resource-intensive

procedure and is therefore unsuitable for multi-dimensional ($N \sim 10^8$) systems such as those considered in the present work. We restrict ourselves to the properties of the leading Lyapunov vector, corresponding to the highest exponent λ_1 . For this purpose, the approach developed by the author in previous publications (Nikitin 2008, 2009) is used. The linearized Navier–Stokes equations for perturbations developing against the background of a developed turbulent flow are integrated in parallel with the equations for the main turbulent flow. With time, the perturbation amplitude goes to an exponential development mode, which corresponds to the output of the solution to the leading Lyapunov vector. A similar method for calculating the evolution of perturbations in a supersonic jet was recently applied in Unnikrishnan & Gaitonde (2016). Formally, the leading Lyapunov vector stands out among the other disturbances only when $t \rightarrow \infty$. However, as shown by our results, even starting with fairly arbitrary random initial conditions, the asymptotic behaviour of the perturbation amplitude $\sim \exp(\lambda_1 t)$ is achieved in a relatively short time $t^+ < 50$. For comparison, the characteristic time of large-scale structures in the near-wall turbulent flow (‘eddy turnover time’) has a larger value of $\tau^+ \approx 80$ (Butler & Farrell 1993).

Numerical studies of the evolution of perturbations in developed turbulent flows were started in Nikitin (2007). It was found that small perturbations introduced in the entrance section of the turbulent pipe flow increase exponentially downstream. In Nikitin (2008) it was shown that in the range of Reynolds numbers Re_τ from 140 to 320 in a pipe and a plane channel, the rate of exponential growth of perturbations corresponds to the universal value $\sigma_1^+ \approx 0.0021$. The growth of perturbations downstream can be interpreted as the growth of perturbations in time during their downstream drift. If c_f is the velocity of drift, then the rate of exponential growth in time can be estimated as $\lambda_1 = c_f \sigma_1$. From the analysis of the propagation of perturbations in Nikitin (2008) was found $c_f^+ \approx 10$ (see also Kim & Hussain 1993), so for the rate of growth in time, the estimate was obtained $\lambda_1^+ \approx 0.021$. This value agrees with the results of Keefe *et al.* (1992), where the Lyapunov spectrum corresponding to turbulent flow in a plane channel was calculated at the extremely low Reynolds number $Re_\tau = 80$. The highest Lyapunov exponent, which characterizes the largest growth rate of small perturbations, turned out to be equal to $\lambda_1^+ \approx 0.02$, which is close to the estimate obtained in Nikitin (2008). Conclusions about the universality (i.e. independence on the Reynolds number and the type of the flow) of λ_1^+ made in Nikitin (2008) were confirmed in Nikitin (2009) by direct calculations of the time evolution of perturbations. In Keefe *et al.* (1992) and Nikitin (2009), the turbulent flows were calculated in the traditional temporal formulation, which assumes the periodicity condition in the longitudinal direction. The condition of spatial periodicity ensures closedness of the system, which justifies the applicability of the approaches of the theory of dynamical systems. In numerical experiments of Nikitin (2008) the system was not closed, since it was supplied with a non-stationary turbulent flow in the pipe’s input section. It is all the more interesting that two fundamentally different approaches from the mathematical point of view give concurring estimates for the maximum rate of growth of perturbations. This, in particular, once again confirms the appropriateness of using periodic boundary conditions in numerical simulations of developed turbulent flows in pipes and channels.

In Inubushi, Takehiro & Yamada (2015), the Lyapunov exponents for the plane Couette flow were calculated at the extremely low Reynolds number $Re = 400$ ($Re_\tau = 34$) in the domain of a minimal size $L_x = 1.75\pi$, $L_z = 1.2\pi$, previously considered in Hamilton *et al.* (1995) (L_x, L_z are the flow dimensions in the longitudinal and lateral directions, respectively). Inubushi *et al.* (2015) obtained $\lambda_1^+ \approx 0.007$ for the

highest Lyapunov exponent, which is three times smaller than the values found in Nikitin (2008, 2009) and Keefe *et al.* (1992). The authors suggest that the reason for such a significant discrepancy is the extremely low value of the Reynolds number in their work. This assumption contradicts the conclusion of Nikitin (2008, 2009) about independence of λ_1^+ from the Reynolds number in near-wall turbulent flows and calls into question the hypothesis of the universality of this characteristic for any near-wall flows. We repeated the calculations of Inubushi *et al.* (2015) and found (Nikitin & Pivovarov 2018) that a noticeable difference in the value of λ_1^+ is due not to the smallness of the Reynolds number, but to the insufficiency of the size of the flow domain. Even with a minimum Reynolds number of $Re = 400$, an increase in the size of the flow domain leads to an increase in λ_1^+ from 0.007 to 0.023, which is close to the estimate $\lambda_1^+ \approx 0.021$, obtained in Nikitin (2008, 2009).

In this paper, the calculation of the highest Lyapunov exponent in a turbulent flow in a plane channel is extended to the region of larger Reynolds numbers (up to $Re_\tau = 586$). In addition, instantaneous manifestations and statistical characteristics of the leading Lyapunov vector are determined. As far as we know, this is the first work on the study of the properties of the leading Lyapunov vector in a realistically calculated near-wall turbulent flow.

2. Formulation of the problem and simulation cases

Consider turbulent velocity fields $\mathbf{u}(t, \mathbf{x})$ and $\mathbf{u}_1(t, \mathbf{x})$ which are close to each other at the initial time $t = 0$. For example, $\mathbf{u}(0, \mathbf{x})$ is the instantaneous velocity distribution in a turbulent flow calculated by direct numerical simulation (DNS), and $\mathbf{u}_1(0, \mathbf{x})$ is $\mathbf{u}(0, \mathbf{x})$ plus a small perturbation:

$$\mathbf{u}_1(0, \mathbf{x}) = \mathbf{u}(0, \mathbf{x}) + \mathbf{u}_p(0, \mathbf{x}), \quad \|\mathbf{u}_p(0, \mathbf{x})\| \ll \|\mathbf{u}(0, \mathbf{x})\|. \quad (2.1a, b)$$

Solving the Navier–Stokes equations with the initial conditions $\mathbf{u}(0, \mathbf{x})$ and $\mathbf{u}_1(0, \mathbf{x})$ in parallel, it is possible to trace the process of divergence of initially close turbulent fields. The evolution of the difference of the two solutions for $t > 0$ can be interpreted as the evolution of perturbation:

$$\mathbf{u}_p(t, \mathbf{x}) = \mathbf{u}_1(t, \mathbf{x}) - \mathbf{u}(t, \mathbf{x}). \quad (2.2)$$

We are interested in the evolution of perturbation, therefore, instead of solving the Navier–Stokes equations for the field \mathbf{u}_1 , it is convenient to rewrite the equations for perturbation (2.2) and solve them in parallel with the equations for \mathbf{u} :

$$\frac{\partial \mathbf{u}}{\partial t} + (\mathbf{u} \cdot \nabla) \mathbf{u} = -\frac{1}{\rho} \nabla p + \nu \nabla^2 \mathbf{u}, \quad \nabla \cdot \mathbf{u} = 0, \quad (2.3)$$

$$\frac{\partial \mathbf{u}_p}{\partial t} + (\mathbf{u}_p \cdot \nabla) \mathbf{u} + (\mathbf{u} \cdot \nabla) \mathbf{u}_p + (\mathbf{u}_p \cdot \nabla) \mathbf{u}_p = -\frac{1}{\rho} \nabla p_p + \nu \nabla^2 \mathbf{u}_p, \quad \nabla \cdot \mathbf{u}_p = 0. \quad (2.4)$$

In (2.4) p_p is the perturbation of the pressure. Equations (2.4) are nonlinear for perturbations developing in the background of the base flow $\mathbf{u}(t, \mathbf{x})$, which in this case is a time-dependent three-dimensional field calculated in parallel by solving equations (2.3).

In this paper we consider a turbulent flow in a plane channel. The Navier–Stokes equations for an incompressible fluid are solved in a rectangular domain $(x, y, z) \in [0, L_x] \times [-h, h] \times [0, L_z]$ with periodicity conditions in homogeneous directions x and

Case	Re (Re_τ)	Grid	L_x/h (L_x^+)	L_z/h (L_z^+)	h_x^+	h_y^+	h_z^+	Δ_{Cf}
R178	5600 (178)	$256 \times 128 \times 256$	12 (2140)	6 (1070)	8.3	1.1–4.3	4.2	−0.2 %
R391	13 764 (391)	$256 \times 256 \times 256$	6 (2350)	3 (1170)	9.2	0.9–4.7	4.6	−0.4 %
R586	21 907 (586)	$512 \times 384 \times 512$	6 (3520)	3 (1780)	6.9	1.0–5.0	3.4	−0.2 %
R391s	13 764 (392)	$64 \times 256 \times 256$	1.5 (590)	3 (1180)	9.2	0.9–4.7	4.6	−0.26 %

TABLE 1. Characteristics of simulation cases. L_x and L_z are the streamwise and spanwise lengths of the computational box and h is the channel half-width; h_x , h_y and h_z are the grid spacings in the streamwise, wall-normal and spanwise directions, respectively; Δ_{Cf} is the difference between the calculated friction coefficient from the value obtained in Moser *et al.* (1999).

z and no-slip conditions on the solid boundaries $y = \pm h$. Nikitin's (2006) algorithm, which combines a conservative second-order-accurate finite-difference method of discretization in space and a third-order semi-implicit Runge–Kutta scheme for time advancement is employed. The bulk velocity of the flow U_b (and, thus, the bulk Reynolds number $Re = 2hU_b/\nu$) is kept constant in simulations. In total, more than 20 simulations have been performed in the course of this investigation within the friction Reynolds number range $140 \leq Re_\tau \leq 590$. Along with the Reynolds number the sizes of flow periods, computational mesh and other algorithmic parameters were also varied.

Three main simulation cases at $Re = 5600$, 13 764 and 21 907 (the corresponding values of the Re_τ are 178, 391 and 586) were selected. The flows at these Reynolds numbers have been simulated earlier by Moser, Kim & Mansour (1999) (detailed data of their simulations are available at http://turbulence.ices.utexas.edu/MKM_1999.html). The calculation parameters, including the friction Reynolds number $Re_\tau = u_\tau h/\nu$, the grid points numbers, the flow periods L_x , L_z and the sizes of computational mesh h_x , h_y , h_z are given in table 1. As is common, the normalization by the wall (viscous) units of velocity $u_\tau = \sqrt{\tau_w/\rho}$ and length ν/u_τ , where τ_w is the mean wall shear stress, ρ and ν are the density and kinematic viscosity of the fluid, is denoted by a superscript '+'. For all the calculations, the grid sizes are adequate for reliable reproduction of the main statistical characteristics of the calculated flows. Mesh size in the longitudinal direction is from 7 to 9 and in the spanwise direction is from 3 to 5 viscous lengths. In the normal to wall direction, the grid spacing at the wall is about one viscous length. The sizes of the computational domain L_x^+ , L_z^+ in all selected cases exceed (sometimes considerably) values of the 2000 and 1000 viscous lengths respectively, which is sufficient for reproducing the most energy-containing structures in the flow.

To represent the degree of accuracy of the simulations the last column of table 1 shows the differences between the calculated friction coefficients from the values obtained in Moser *et al.* (1999). A maximum deviation of 0.4 % indicates the high quality of our simulations. Note that a good agreement with the results of Moser *et al.* (1999) is observed for all the characteristics they present. To exemplify, figures 1 and 2 show the profiles of mean velocity and root-mean-square (r.m.s.) velocity and vorticity intensities at a maximum Reynolds number of $Re_\tau = 586$. The results obtained in this work with graphic accuracy coincide with the results of Moser *et al.* (1999), which is additional evidence of the accuracy of the calculations. In figures 1, 2 and hereafter the components of the velocity \mathbf{u} and vorticity $\nabla \times \mathbf{u}$ of the main flow are denoted as $(u_1, u_2, u_3) \equiv (u, v, w)$ and $(\omega_1, \omega_2, \omega_3) \equiv (\omega_x, \omega_y, \omega_z)$, respectively.

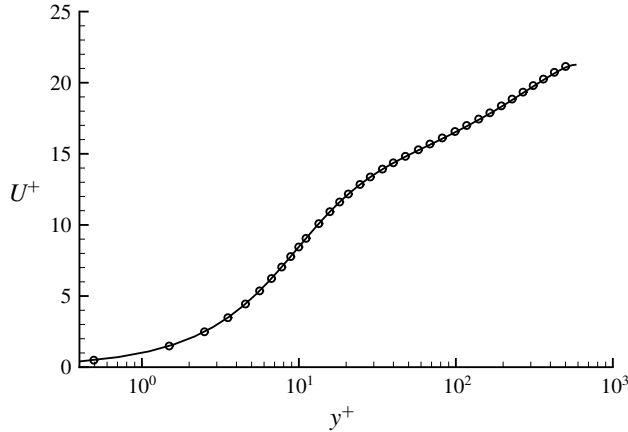


FIGURE 1. $Re_\tau = 586$. Mean-velocity profile: line, simulation by Moser *et al.* (1999); symbols, present simulation.

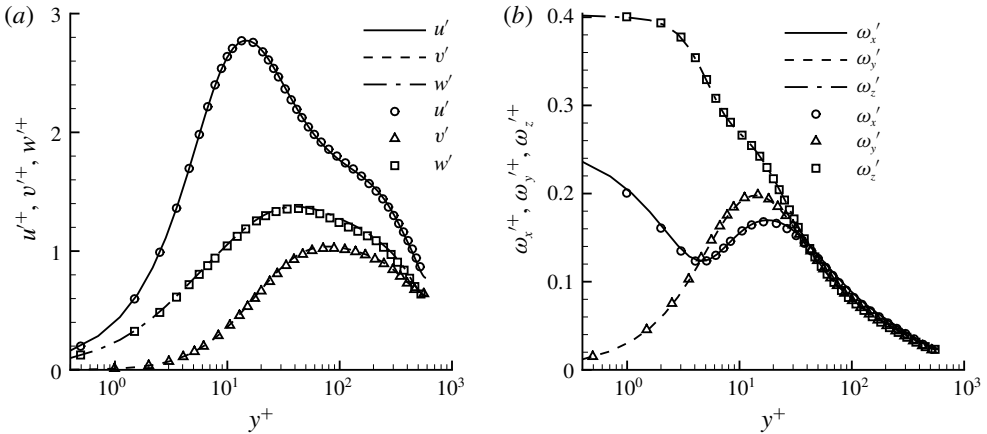


FIGURE 2. $Re_\tau = 586$. Root-mean-square intensities of (a) velocity and (b) vorticity fluctuations: lines, simulation by Moser *et al.* (1999); symbols, present simulation.

Similarly, the components of the velocity and vorticity perturbations \mathbf{u}_p and $\nabla \times \mathbf{u}_p$ are denoted as $(u_{1,p}, u_{2,p}, u_{3,p}) \equiv (u_p, v_p, w_p)$ and $(\omega_{1,p}, \omega_{2,p}, \omega_{3,p}) \equiv (\omega_{x,p}, \omega_{y,p}, \omega_{z,p})$. When referring to the perturbations described by the linearized equations (3.6) subscript p is replaced by the l .

In addition to three main cases, the case R391s will be considered. This simulation differs from R391 by the decreased length of the computational domain $L_x^+ \approx 590$, with a proportional decrease in the number of grid nodes in the x -direction. Despite the short computational domain, the calculation results of the case R391s are qualitatively and quantitatively close to those of the R391. The friction coefficients in the two flows differ by 0.14%. The differences in the mean velocity do not exceed 5%, and in the r.m.s. fluctuation intensities, 10%. As will be shown in §4, the growth rate of small perturbations in these two flows also coincide with a high accuracy. The reduced domain in the R391s case is used for the flow decomposition into streaky and short-wave components. Following Jiménez & Pinelli (1999) the streaky component

is considered not to be dependent on x and is calculated by averaging of the flow field over the length of the computational domain. The rest refers to the short-wave component.

In what follows, the results obtained for the R391 case, which received the most attention, are presented. The results for the lower and higher Reynolds numbers were used mainly to confirm the qualitative findings.

3. Characteristics of growing perturbations

Numerical investigations of spatial evolution of perturbations in developed turbulent flows were initiated by Nikitin (2007). This and subsequent papers Nikitin (2008, 2009) showed that small perturbations in a circular pipe and plane channel grow, on average, exponentially in x , when spatial development is simulated, and in time, when the problem is solved in a temporal formulation with condition of spatial periodicity. It should be noted that the procedure of the adopted approach ensures the isolation from all others only the fastest growing perturbation. For chaotic systems, this perturbation corresponds to the leading Lyapunov vector (corresponding to the highest Lyapunov exponent λ_1). In contrast to the eigenvectors of the problem of stability of stationary solutions, Lyapunov vectors randomly vary in time, so that their properties are determined only statistically. So, in this paper we study the properties of the leading Lyapunov vector only. The question of the presence and the number of other growing Lyapunov vectors (the number of positive Lyapunov exponents) is not considered in this paper.

3.1. Rate of growth

The results of the present simulations are consistent with those of Nikitin (2007, 2008, 2009). Small perturbations in the turbulent flow after the initial adjustment grow, on average, exponentially. General exponential trend is maintained until saturation at a certain finite-amplitude level. The specific form of initial perturbation affects only the initial stage of perturbation development but does not affect the rate of exponential growth. In the present work, initial perturbations were set randomly (using a random numbers generator), followed by conversion of the velocity field to a divergence-free form and normalization. Figure 3 shows the time evolution of the integral perturbation amplitude ε_p , defined as

$$\varepsilon_p^2(t) = \frac{1}{|V|} \int_V |\mathbf{u}_p(t, \mathbf{x})|^2 d\mathbf{x}. \quad (3.1)$$

The integration in (3.1) is performed over the whole computational domain with a volume of $|V|$. In figure 3(a) time is measured in global units h/U_0 , where h is the channel half-width, and $U_0 = 1.5U_b$ is the maximum velocity of the Poiseuille flow corresponding to the bulk velocity U_b . A random choice of initial perturbation results in appreciable attenuation (by an order of magnitude or more) in the initial stage of evolution. In all the simulations, when the initial amplitude was set to $\varepsilon_p(0)/U_0 = 10^{-10}$ the decay of the perturbations on the initial stage gives way to exponential growth which continues until saturation on the level $\varepsilon_p/U_0 \approx 10^{-1}$. The rate of exponential growth increases with the Reynolds number.

In Nikitin (2008, 2009) it was found that in the Reynolds number range Re_τ from 140 to 320, the growth rate of small perturbations being expressed in wall units is close to the constant $\lambda_1^+ \approx 0.021$. The results of this paper, agree with the constancy of λ^+ in the Re_τ range from 140 to 320, but show an increase in λ_1^+ for greater Reynolds numbers. Figure 3(b) shows the graphs $\varepsilon_p(t^+)$ showing some change in the slope of the growth curves with increasing Re .

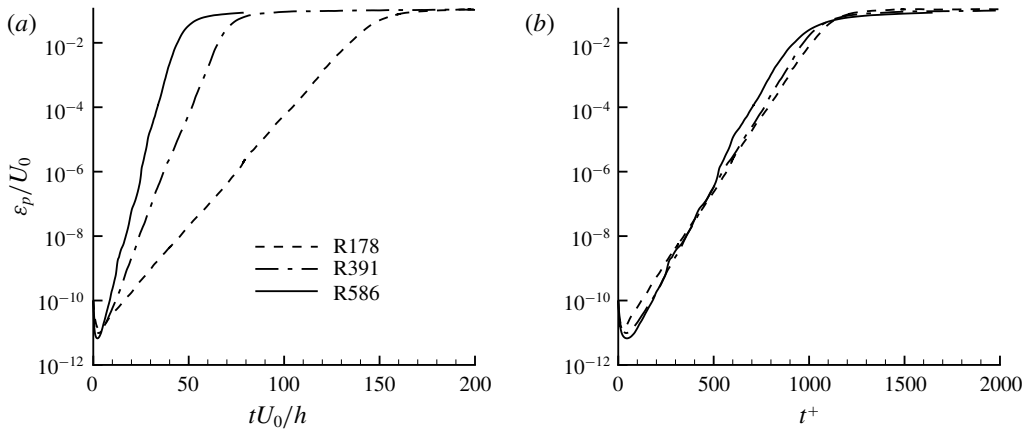


FIGURE 3. Evolution of perturbation amplitude. Perturbations grow exponentially in the linear stage and nonlinearly saturate on a level of $\varepsilon_p/U_0 \approx 10^{-1}$. The rate of exponential growth increases with the Reynolds number when time is measured in global units h/U_0 and is close to a constant with a slight increase with Re when time is measured in wall units, $t^+ = tu_\tau^2/\nu$.

3.2. The structure of the perturbation field after the completion of the stage of nonlinear saturation

In the initial moment of time the perturbed field $\mathbf{u}_1 = \mathbf{u} + \mathbf{u}_p$ differs from the original field \mathbf{u} to a small value, but the degree of divergence of the two fields increases with the growth of the perturbation. The increase of the disturbance amplitude up to the limit value suggests that the phase of divergence of the two fields has completed and the field \mathbf{u}_1 has reached the state of statistical independence from the original field \mathbf{u} . In other words, the fields \mathbf{u} and \mathbf{u}_1 at this limiting stage represent two statistically independent realizations of the same stationary turbulent flow and thus have identical statistical characteristics. It follows from this that mean values of perturbation \mathbf{u}_p are identically equal to zero: $\overline{u_{i,p}}(y) = 0$. Henceforth the overline denotes averaging over the time and homogeneous coordinates x and z .

To determine the second moments of the perturbation field let us consider the following cross-correlation of the two components of the perturbation velocity $u_{i,p}$ and $u_{j,p}$:

$$C_{ij,p}(y; \Delta_x, \Delta_z) = \overline{u_{i,p}(t, x, y, z)u_{j,p}(t, x + \Delta_x, y, z + \Delta_z)}. \quad (3.2)$$

In the last expression we substitute the definition of the perturbation (2.2), which, taking into account the equality of the mean values $\overline{\mathbf{u}_1} = \overline{\mathbf{u}}$, is written as the difference of the fluctuation components of the fields \mathbf{u} and \mathbf{u}_1 :

$$\mathbf{u}_p(t, \mathbf{x}) = (\mathbf{u}_1(t, \mathbf{x}) - \overline{\mathbf{u}_1}(y)) - (\mathbf{u}(t, \mathbf{x}) - \overline{\mathbf{u}}(y)). \quad (3.3)$$

Taking into account also the statistical independence and the coincidence of the statistical characteristics of the fields \mathbf{u} and \mathbf{u}_1 by simple manipulations, we obtain

$$C_{ij,p}(y; \Delta_x, \Delta_z) = 2C_{ij}(y; \Delta_x, \Delta_z), \quad (3.4)$$

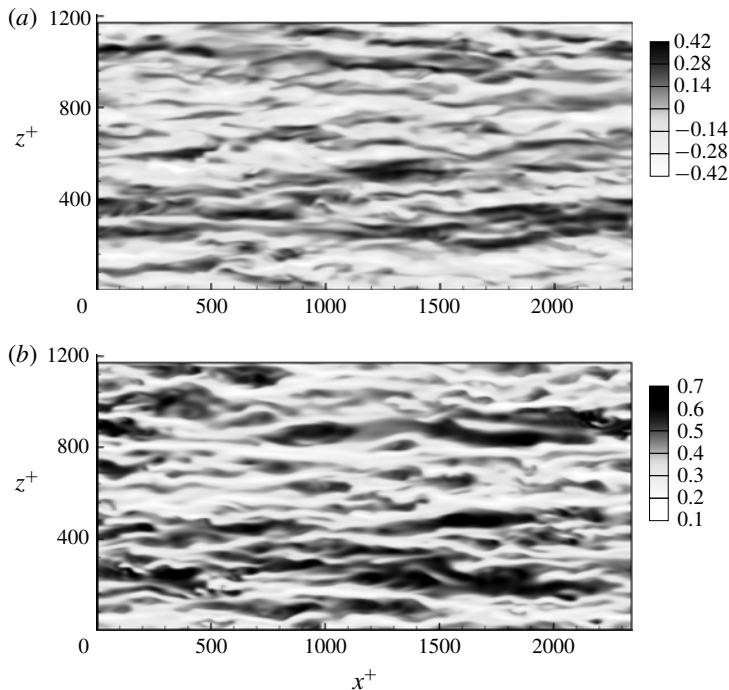


FIGURE 4. $Re_\tau = 391$. The distribution of longitudinal velocity in the plane $y^+ = 14$: (a) perturbation field after reaching the limiting state; (b) base flow. Perturbation field after completing the nonlinear transformations in each horizontal plane is structurally identical to the base flow. In particular, similar streaky structures are present in both fields. Mean values in perturbation field are zero, and the spread of fluctuations is $\sqrt{2}$ times greater than that in the base flow in accordance with (3.5).

where $C_{ij}(y; \Delta_x, \Delta_z) = \overline{(u_i(t, x, y, z) - \bar{u}_i(y))(u_j(t, x + \Delta_x, y, z + \Delta_z) - \bar{u}_j(y))}$ is the cross-correlation of the velocity pulsations in the base turbulent flow. In particular substituting $\Delta_x = \Delta_z = 0$ in (3.4) we obtain the expressions for the perturbation Reynolds stresses $\overline{u_{i,p}u_{j,p}}$ and the r.m.s. perturbation intensities $u'_{i,p} = \sqrt{\overline{u_{i,p}u_{i,p}}}$ as follows:

$$\overline{u_{i,p}u_{j,p}}(y) = 2\overline{(u_i - \bar{u}_i)(u_j - \bar{u}_j)}(y), \quad u'_{i,p}(y) = \sqrt{2}u'_i(y). \quad (3.5a,b)$$

It is obvious that similar equations are valid for the vorticity components. The calculated second moments of the velocity and vorticity fluctuations, corresponding to the perturbation field on the limiting stage after its nonlinear saturation, satisfy the relations (3.5) with high accuracy. This proves the assumption that there is statistical independence of the fields \mathbf{u} and \mathbf{u}_1 at this stage.

The correlation functions are linearly related to the spatial spectra of the fluctuations by the Wiener–Khinchine formula. Thus, the coincidence (up to a multiplier) of cross-correlation functions corresponding to fluctuations in the perturbation field and in the field of the base flow indicates a similar coincidence of spatial spectra. All this points to the fact that in the limiting field of perturbation the same structures that appear in the base flow are present. Figure 4 depicts the instantaneous distributions of the

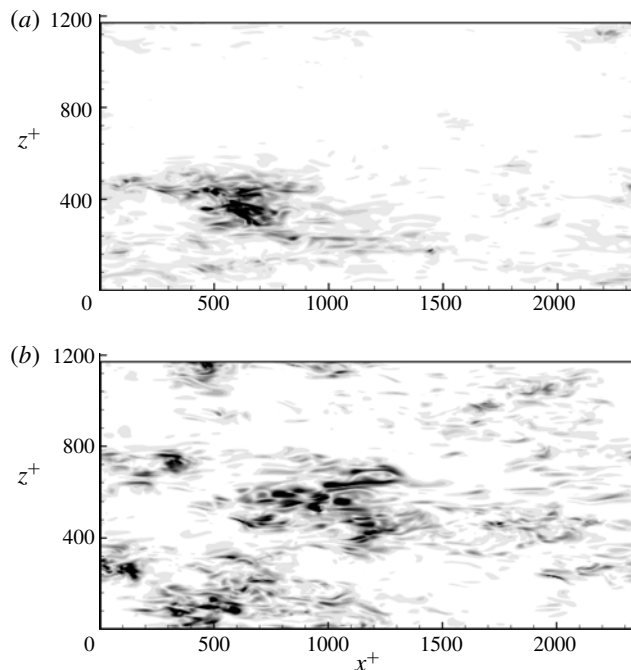


FIGURE 5. $Re_\tau = 391$. Distribution of perturbation intensity $\sqrt{|\mathbf{u}_p|^2}$ in the plane $y^+ = 14$ at random times at a linear stage of development. Spatially localized random bursts of activity sporadically appear and disappear in different places of the channel. Characteristic scales of perturbation structures are considerably smaller than that of the structures in the base flow or of those that occur in the perturbation field in the limiting state after nonlinear saturation (see figure 4).

longitudinal velocity in the horizontal plane $y^+ = 14$ in the limiting perturbation field and in the base flow. The two fields are qualitatively similar which is in accordance with the predictions. In particular, large-scale elongated streaky structures are clearly visible in both fields. Moreover, in accordance with (3.5), the spread of values in the perturbation field is $\sqrt{2}$ times greater than that of the base flow.

3.3. Spatial localization of growing perturbations

Observing the development of small perturbations in the linear stage, it can be seen that evolution occurs in the form of spatially localized random bursts of activity that sporadically appear and disappear in different places of the channel. The greatest activity is observed at a height of $y^+ = 10\text{--}20$, i.e. in the region of the buffer layer of the base flow. Spatially localized perturbation structure after appearing grows transiently in size and intensity while moving downstream, thereby increasing the integral amplitude of the perturbation. The distributions of the perturbation intensity $\sqrt{|\mathbf{u}_p|^2}$ in the plane $y^+ = 14$ in two random time instants shown in figure 5 demonstrate the degree of spatial inhomogeneity of the perturbation field as well as some characteristic geometric features of the excited perturbation structures. In particular, it is noteworthy that despite the elongation of the perturbation patterns along the stream, there are no large-scale structures resembling near-wall streaks in

the main turbulent flow or those that occur in the perturbation field in the limiting state after nonlinear saturation (see figure 4).

In Egolf *et al.* (2000), the so-called chaotic regime of spiral defects in Rayleigh–Bénard convection was numerically studied. It was found that the Lyapunov vectors corresponding to positive exponents are extremely localized both in space and in time. On the contrary, the Lyapunov vectors corresponding to negative exponents are more evenly distributed in space. It was concluded that the appearance of chaos in the investigated regime is associated with bursts of pulsation activity described by the leading Lyapunov vector. In the boundary layer flows, spatially localized turbulent spots are encountered at the laminar–turbulent transition stage. Recently, Wu *et al.* (2017) detected spatially localized formations with increased pulsating activity in the buffer layer of a developed turbulent boundary layer. In their properties they resemble turbulent spots in transitional flows. It is interesting that the near-wall streaks look inactive in relation to the localized structures developing against their background. The spatio-temporal localization of perturbations corresponding to the leading Lyapunov vector found in the present study agrees with the observations and conclusions of Egolf *et al.* (2000) and resembles the localized turbulent structures of the developed boundary layer found in Wu *et al.* (2017). In the framework of this study, attempts have been made to establish the connection between the circumstances of sudden outbreaks of perturbations activity and the characteristics of the field of the base flow, in particular, with details of large-scale streaky structures. So far, certain conclusions on this path have not been made. As in the numerical experiments of Wu *et al.* (2017), the instantaneous distribution of near-wall streaks does not seem to be an important factor in the growth of perturbations. Probably, not only the spatial inhomogeneity, but also the non-stationary nature of the base flow, has a significant effect on the growth conditions of the perturbations, as noted in the works of Farrell & Ioannou (2012); Farrell *et al.* (2016). In addition, as will be shown below, the short-wave component of the base flow, and also the motion in the transverse plane to the direction of the main stream, make a serious contribution to the development of perturbations.

3.4. Statistical characteristics of small perturbations

In § 3.2 it was shown that the statistical properties of the perturbation after completing the stage of nonlinear saturation are associated with the properties of the underlying turbulent flow. To determine the characteristics of the small growing perturbation we neglect the nonlinear term $(\mathbf{u}_p \cdot \nabla) \mathbf{u}_p$ in the left-hand side of the first of equations (2.4). To avoid confusion with solutions of the nonlinear equations (2.4) the solutions of the obtained linear equations are denoted by \mathbf{u}_l :

$$\frac{\partial \mathbf{u}_l}{\partial t} + (\mathbf{u}_l \cdot \nabla) \mathbf{u} + (\mathbf{u} \cdot \nabla) \mathbf{u}_l = -\frac{1}{\rho} \nabla p_l + \nu \nabla^2 \mathbf{u}_l, \quad \nabla \cdot \mathbf{u}_l = 0. \quad (3.6)$$

The solutions of these equations at the initial stage coincide with the solutions of (2.4). However, after the reaching the exponential regime they remain there without saturation for an infinitely long time. A longer period of development makes it possible to more accurately estimate the rate of perturbation growth. The graphs of the integral perturbation amplitude $\varepsilon_l(t^+)$, defined similarly as in (3.1) via \mathbf{u}_l , obtained for the three main simulation cases are shown in figure 6. The solutions of the linear problem are determined to within an arbitrary factor, so that the normalization of the initial perturbation can also be chosen arbitrarily. In these calculations, the normalization is chosen based on the condition $\varepsilon_l(0)/U_0 = 1$. The graphs shown

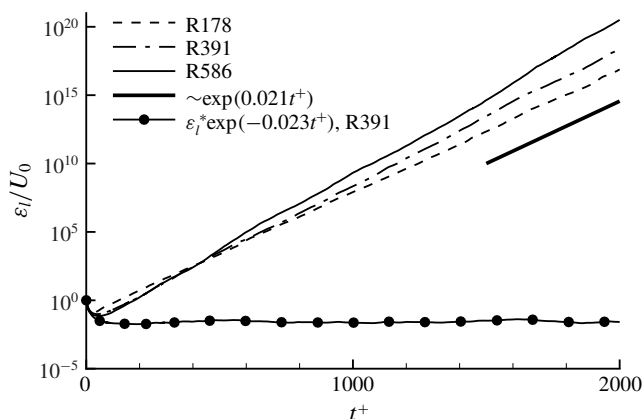


FIGURE 6. Evolution of the perturbation amplitude governed by the linear equation (3.6). The normalization is chosen based on the condition $\varepsilon_l(0)/U_0 = 1$. Perturbation growth rate increases with Reynolds number from $\lambda_1^+ = 0.021$ at $Re_\tau = 178$ to $\lambda_1^+ = 0.026$ at $Re_\tau = 586$.

in figure 6 clearly display an increase in the rate of exponential growth of the perturbation amplitude from $\lambda_1^+ = 0.021$ at $Re_\tau = 178$ to $\lambda_1^+ = 0.026$ at $Re_\tau = 586$. At $Re_\tau = 391$, the best estimate is $\lambda_1^+ = 0.023$, which is confirmed by the absence of a noticeable exponential trend on the graph $\varepsilon_l(t^+) \exp(-0.023t^+)/U_0$. Note that the exponential dependency $\varepsilon_l \sim \exp(\lambda_1 t)$ is reached in all variants already when $t^+ < 50$ despite the randomness of the initial perturbation.

It seems natural to assume that the qualitative properties of small perturbations remain unchanged during the entire time of exponential growth, and the normalized field

$$\hat{u}_l(t, \mathbf{x}) = \mathbf{u}_l(t, \mathbf{x}) \exp(-\lambda_1 t) \quad (3.7)$$

evolves as a statistically stationary process. The statistical characteristics presented below were obtained by averaging over the time and homogeneous spatial coordinates of the various perturbation quantities corresponding to the normalized field (3.7). Thus, these characteristics depend only on the wall-normal coordinate and are determined to within an arbitrary factor reflecting the arbitrariness of the initial level of the perturbation. Technically, the statistics are calculated in two stages. At the first stage, the perturbation growth rate λ_1 is determined by integrating the linearized equations (3.6) and analysing the behaviour of the perturbation amplitude $\varepsilon_l(t)$. Then the calculation is repeated, but at each integration step the solution is renormalized in accordance with (3.7), and the various statistics of $\hat{u}_l(t, \mathbf{x})$ are calculated by integrating over time and averaging over x and z .

The r.m.s. intensities (u'_l , v'_l , w'_l) of velocity fluctuations of the linearly growing perturbations, obtained by the above method, are shown in figure 7(a). In the same figure, for comparison, we show analogous characteristics (u' , v' , w') in the base flow. The normalization of the perturbation is chosen based on the condition that the maximum intensities of velocity fluctuations in the transverse plane are equal in the perturbation field and in the field of the base flow:

$$\max_y \{(v'_l)^2 + (w'_l)^2\} = \max_y \{(v'^+)^2 + (w'^+)^2\}. \quad (3.8)$$

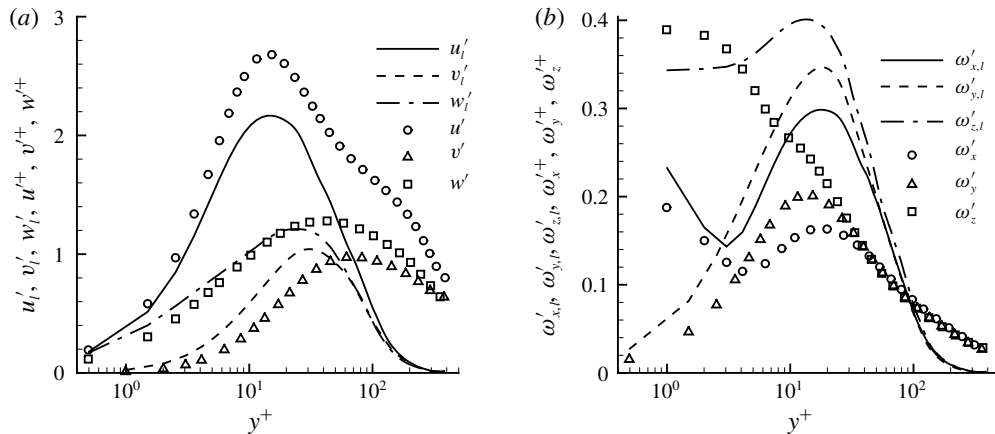


FIGURE 7. $Re_\tau = 391$. Root-mean-square intensities of (a) velocity and (b) vorticity fluctuations: lines, perturbations in the linear stage of development; symbols, base flow. Normalization of perturbations is in accordance with (3.8).

The maximum pulsations in the perturbation field are concentrated in the region $y^+ \approx 14$, where, in particular, the streaks in the base flow are most pronounced. The latter may mean that the growth of perturbations is a consequence of the instability of the streaky motion. However, as will be shown below, the instability of the streaks is not the main cause of the growth of the perturbations of the leading Lyapunov vector. In accordance with the chosen normalization, the maximum pulsation intensities of the spanwise and normal components of the perturbation velocity are close to the corresponding values in the base flow. In contrast, the intensity of longitudinal fluctuations in the base flow is considerably higher than in the perturbation field. We believe that this difference occurs owing to the presence of high-amplitude large-scale streaks in the base flow, which makes an appreciable contribution to the intensity of longitudinal velocity fluctuations in the near-wall layer of the turbulent flow. In general, the disturbances turn out to be much more concentrated along the thickness of the channel. The intensities of the velocity fluctuations in the perturbation field decays much more rapidly when moving away from the region of maximum values than in the field of the base flow.

The intensities of vorticity fluctuations shown in figure 7(b) have several interesting features. The profiles $\omega'_{x,l}$ and $\omega'_{y,l}$ corresponding to the longitudinal and normal vorticity components in the perturbation field are qualitatively close to similar profiles $\omega_x^{'+}$ and $\omega_y^{'+}$ constructed for the base flow. However, the $\omega'_{z,l}$ profile differs significantly from $\omega_z^{'+}$. The pulsations of ω_z in the base flow reaches a maximum directly on the wall and monotonically decreases with distance from it. In contrast, the perturbation intensity $\omega'_{z,l}$ is maximal at the same distance from the wall, $y^+ = 10\text{--}20$, as for the other vorticity components. Directly on the wall $\omega_z = -\partial u/\partial y$, therefore large fluctuations of the longitudinal velocity due to the presence of streaky structures in the wall layer obviously cause fluctuations of ω_z directly on the wall and near it. Hence, the qualitative difference between $\omega'_{z,l}$ and $\omega_z^{'+}$ near the wall can also be explained by the presence of streaky motion in the base flow and its absence in the perturbation field.

The validity of the assumptions about the contribution of streaky structures to the intensity profiles of velocity and vorticity fluctuations can be verified using the results

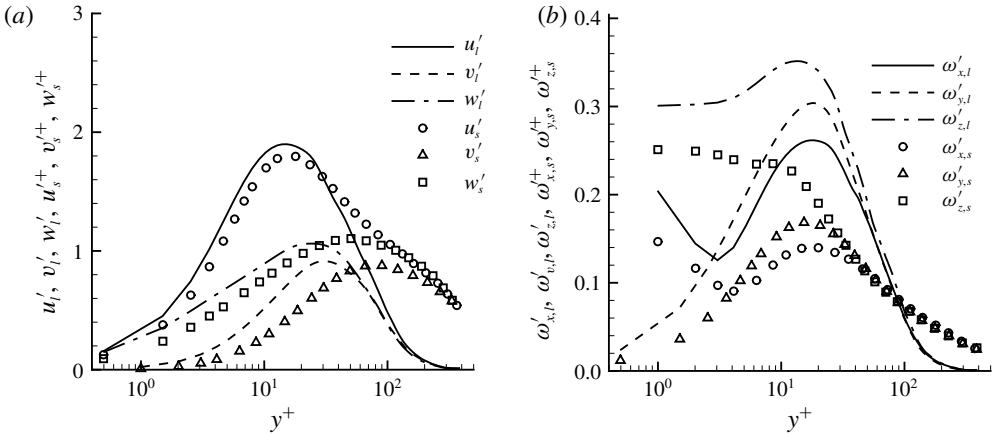


FIGURE 8. $Re_\tau = 391$. Root-mean-square intensities of (a) velocity and (b) vorticity fluctuations: lines, perturbations in the linear stage of development; symbols, short-wave component $\mathbf{u}_s = \mathbf{u} - \langle \mathbf{u} \rangle_x$ of the base flow of calculation R391s. Normalization of perturbations is in accordance with (3.9).

of calculations in the truncated calculation region (R391s in table 1). The length of the simulation domain in this variant $L_x^+ \approx 590$ is less than the typical length of near-wall streaks in the turbulent flow. Thus, most of the streaks in this calculation are stretched along the stream over the entire length of the simulation domain. Then, the short-wave component of the flow $\mathbf{u}_s = (u_s, v_s, w_s)$ obtained by excluding from the flow field the x -independent component: $\mathbf{u}_s = \mathbf{u} - \langle \mathbf{u} \rangle_x$ ($\langle \cdot \rangle_x$ means averaging over x), can be considered as almost free of streaks. In figure 8, the perturbation intensities from simulation case R391 are compared with the velocity and vorticity intensities (u'^+_s, v'^+_s, w'^+_s) and ($\omega'^+_{x,s}, \omega'^+_{y,s}, \omega'^+_{z,s}$) of the short-wave component of the motion, obtained in the calculation R391s. The perturbations are normalized similarly to (3.8) as follows:

$$\max_y \{(v'_l)^2 + (w'_l)^2\} = \max_y \{(v'^+_s)^2 + (w'^+_s)^2\}. \quad (3.9)$$

As expected, the elimination of the long-wave component is primarily reflected in a decrease in the level of longitudinal velocity fluctuations in the region $y^+ = 10$ – 20 and the fluctuations ω_z in the immediate vicinity of the wall. As a result, we obtain a closer quantitative agreement between u'_l and u'^+_s as well as a better qualitative agreement between $\omega'_{z,l}$ and $\omega'^+_{z,s}$. This supports the conclusion about the absence of high-amplitude large-scale streaks in the perturbation field in the linear stage of development.

With normalizations (3.8) and (3.9), the characteristic values of the vorticity fluctuations in the perturbation field are approximately 80% greater than the values in the base flow. This may be explained by the fact that these fluctuations are associated with vortices having a smaller linear size. This is indirectly confirmed by the greater y -localization of the intensity of velocity and vorticity perturbations as shown in figures 7 and 8. The following analysis of spatial spectra provides more convincing arguments in favour of the dominating of smaller-size structures in the perturbation field.

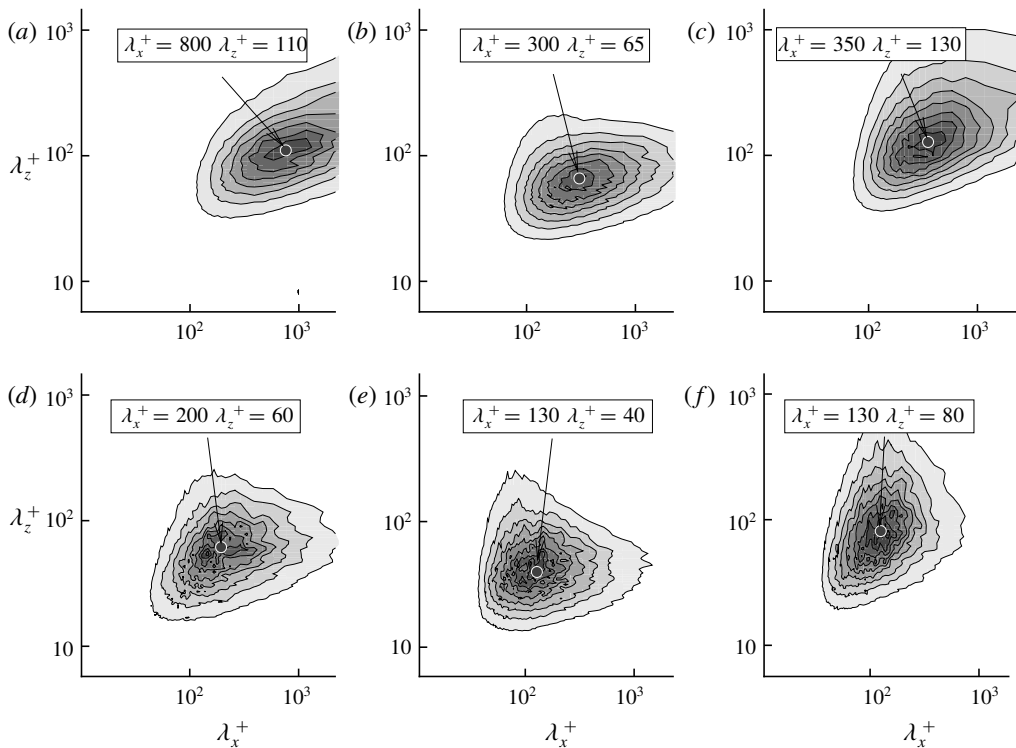


FIGURE 9. $Re_\tau = 391$. Premultiplied two-dimensional spectra of velocity fluctuations $k_x k_z E_{u_i u_i}$ at distance $y^+ = 14$ from the wall: (a–c) in the base flow; (d–f) in the perturbation in the linear stage of development. From left to right: u , v and w components. Boxed are the coordinates of maxima.

Figure 9 depicts the premultiplied two-dimensional spectra of the three components of velocity $k_x k_z E_{u_i u_i}(k_x, k_z)$ in the base flow and in the perturbation field at $y^+ = 14$, i.e. in the region of maximum fluctuation level in both fields. The spectra are represented as functions of the logarithms of the wavelengths $\lambda_x = 2\pi/k_x$, $\lambda_z = 2\pi/k_z$. With this representation, the oscillation energy per elementary area $d(\ln \lambda_x) d(\ln \lambda_z)$ is proportional to the level of the pictured value $k_x k_z E_{u_i u_i}$, since

$$k_x k_z E_{u_i u_i}(k_x, k_z) d(\ln \lambda_x) d(\ln \lambda_z) = 4\pi^2 E_{u_i u_i}(k_x, k_z) dk_x dk_z. \quad (3.10)$$

In particular, the coordinates of the maximum levels of the premultiplied spectra indicate the characteristic dimensions (wavelengths) of the most-energy-containing structures. These coordinates are shown in each of the graphs in figure 9.

Two-dimensional spectra of velocity fluctuations show that the length of the simulation domain $L_x^+ = 2350$ is not completely sufficient for accurate reproduction of all the energy-containing structures in the base flow. This is most relevant to the longitudinal velocity component. This, however, does not mean that the long structures are not considered in the simulations. They are represented by the structures independent of x , i.e. by the spectral components corresponding to $k_x = 0$. Perturbations are better resolved by the computational grid in both the maximum and the minimum resolved size. In general, the most energy-containing structures in the perturbation field are narrower and shorter than those in the base flow.

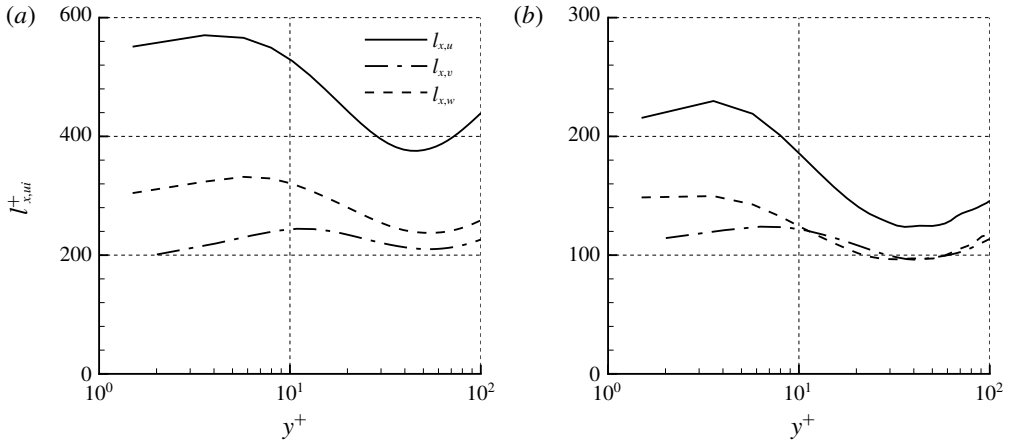


FIGURE 10. $Re_\tau = 391$. Characteristic longitudinal scales of velocity fluctuations (3.11): (a) in the base flow; (b) in the perturbations in the linear stage of development.

For more objective estimation of the sizes of the various structures in the base flow and in the perturbation fields, we introduce characteristic velocity linear scales $l_{x,u_i}(y)$, $l_{z,u_i}(y)$ in the longitudinal and lateral directions:

$$2\pi l_{x,u_i}^{-1}(y) = \frac{\iint k_x E_{u_i u_i}(k_x, k_z; y) dk_x dk_z}{\iint E_{u_i u_i}(k_x, k_z; y) dk_x dk_z}, \quad (3.11)$$

$$2\pi l_{z,u_i}^{-1}(y) = \frac{\iint k_z E_{u_i u_i}(k_x, k_z; y) dk_x dk_z}{\iint E_{u_i u_i}(k_x, k_z; y) dk_x dk_z}. \quad (3.12)$$

Similarly, we define the characteristic linear scales of the vorticities $l_{x,\omega_i}(y)$, $l_{z,\omega_i}(y)$ in terms of the power spectra of the vorticity fluctuations $E_{\omega_i \omega_i}(k_x, k_z; y)$. Figures 10–13 show the characteristic scales corresponding to the different velocity and vorticity components in the base flow and perturbations as functions of the distance from the wall in the near-wall layer $y^+ \leq 10^2$.

Figures 10–13 reveal the interesting geometric properties inherent in structures in the two fields. For any velocity or vorticity component, the distribution across the channel of each of the two linear scales in the perturbation field is surprisingly close in form to the corresponding distribution in the field of the base flow. However, the value of each linear scale in the perturbation field turns out to be half that of the corresponding scale in the field of the base flow. In the region of maximum fluctuations, $y^+ = 10$ – 20 , the longitudinal scale in the perturbation field is 100–150, while in the base flow it is 200–300 viscous lengths. For a lateral scale, analogous values for different components of velocity and vorticity are two or three times smaller. The longitudinal length scale of streamwise velocity in the base flow is considerably larger than the doubled value of the corresponding quantity in the perturbation field, which is most likely a reflection of the presence of streaky structures in the base flow. For the same reason, the longitudinal scale of the spanwise vorticity in the base flow

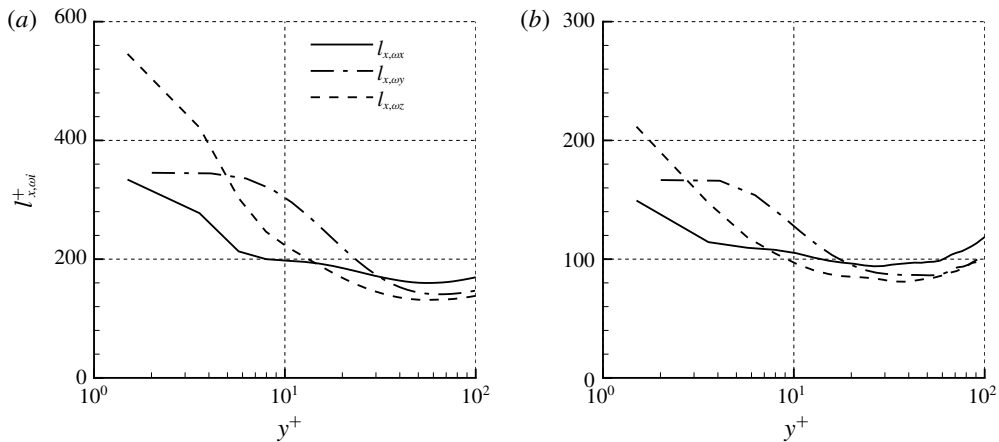


FIGURE 11. $Re_\tau = 391$. Characteristic longitudinal scales of vorticity fluctuations: (a) in the base flow; (b) in the perturbations in the linear stage of development.

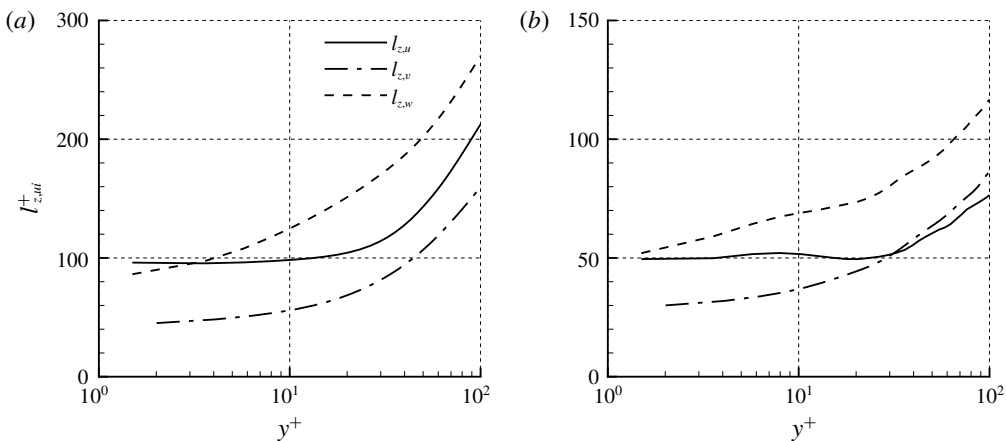


FIGURE 12. $Re_\tau = 391$. Characteristic lateral scales of velocity fluctuations (3.12): (a) in the base flow; (b) in the perturbations in the linear stage of development.

in the immediate vicinity of the wall also significantly exceeds the doubled value of the corresponding quantity in the perturbation field.

The integral scales determined in (3.11), (3.12) calculated through the energy spectra should not be taken literally as the geometric dimensions of the structures existing in the flow (see Hutchins & Marusic 2007). We note, however, in particular that the longitudinal scale of the axial vorticity l_{x,ω_x}^+ in the region of concentrated streaky structures $y^+ = 10$ – 20 in the base flow is about 200 units (see figure 11). This coincides with the length of the quasi-streamwise vortices defined in Jeong *et al.* (1997), who used vortex identification method of Jeong & Hussain (1995). This indicates that the values formally introduced in (3.11), (3.12) actually may be considered as linear scales of turbulent structures.

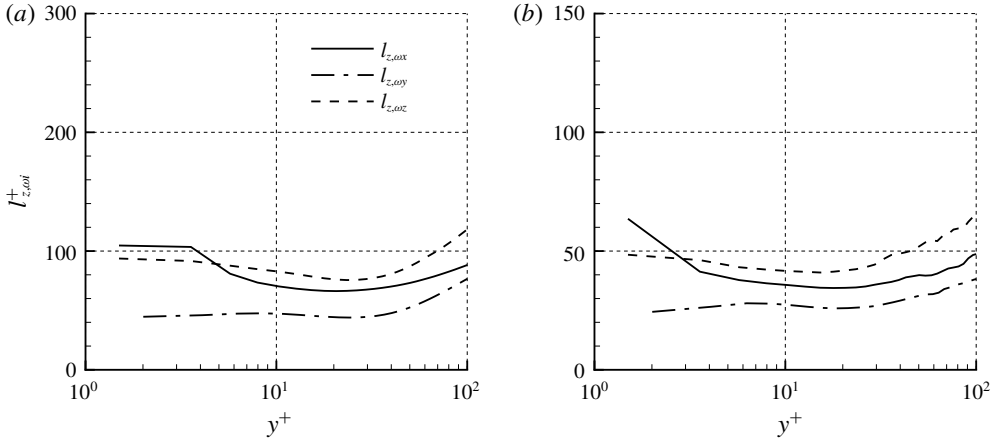


FIGURE 13. $Re_\tau = 391$. Characteristic lateral scales of vorticity fluctuations: (a) in the base flow; (b) in the perturbations in the linear stage of development.

4. On the mechanism of generation of perturbations

A certain understanding of the importance of different mechanisms for generating perturbations in a turbulent flow gives an analysis of the kinetic energy budget. To derive the equation for the energy budget of small perturbations at the linear stage of development, we multiply (3.6) by $\mathbf{u}_l = (u_l, v_l, w_l) \equiv (u_{1,l}, u_{2,l}, u_{3,l})$. After simple transformations, we get:

$$\frac{\partial}{\partial t} \left(\frac{1}{2} u_{i,l} u_{i,l} \right) = -u_{i,l} u_{j,l} s_{ij} - \frac{\partial}{\partial x_j} \left(\frac{1}{2} u_{i,l} u_{i,l} u_j + \frac{1}{\rho} u_{j,l} p_l - 2\nu u_{i,l} s_{ij,l} \right) - 2\nu s_{ij,l} s_{ij,l}. \quad (4.1)$$

Here,

$$s_{ij} = \frac{1}{2} \left(\frac{\partial u_i}{\partial x_j} + \frac{\partial u_j}{\partial x_i} \right), \quad s_{ij,l} = \frac{1}{2} \left(\frac{\partial u_{i,l}}{\partial x_j} + \frac{\partial u_{j,l}}{\partial x_i} \right) \quad (4.2a,b)$$

are the rate of strain tensors of the base flow and perturbation, respectively. We then multiply (4.1) by $\exp(-2\lambda_1 t)$ and average each term with respect to time and homogeneous coordinates x and z . As a result, we get

$$2\lambda_1 K_l = P_l + T_l - D_l. \quad (4.3)$$

Here, $P_l(y)$, $T_l(y)$ and $D_l(y)$ are the production, transport and dissipation of the kinetic energy of the perturbation $K_l(y)$ which are determined by the following formulas (Tennekes & Lumley 1972):

$$K_l = \frac{1}{2} \overline{\hat{u}_{i,l} \hat{u}_{i,l}}, \quad P_l = -\overline{\hat{u}_{i,l} \hat{u}_{j,l} s_{ij}}, \quad (4.4a,b)$$

$$T_l = -\frac{d}{dy} \left(\frac{1}{2} \overline{\hat{u}_{i,l} \hat{u}_{i,l} v} + \frac{1}{\rho} \overline{\hat{v}_l \hat{p}_l} - 2\nu \overline{\hat{u}_{i,l} \hat{s}_{i2,l}} \right), \quad D_l = 2\nu \overline{\hat{s}_{ij,l} \hat{s}_{ij,l}}. \quad (4.5a,b)$$

We recall that hats over perturbation quantities denote the normalization (3.7).

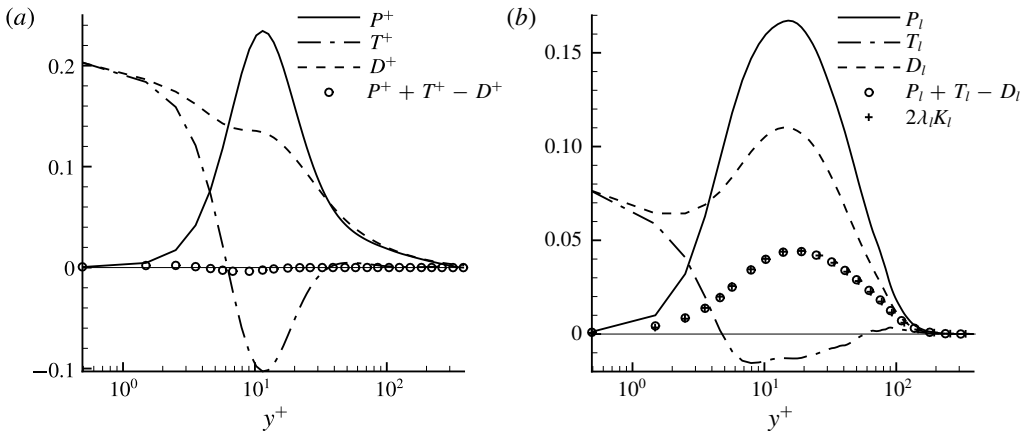


FIGURE 14. $Re_\tau = 391$. The terms of the equation of the fluctuating kinetic energy budget: (a) base flow; (b) perturbation field in the linear stage of development. P, P_l , production; T, T_l , transport; D, D_l , dissipation. Definitions are given in (4.4), (4.5).

The profiles of all the terms of the energy budget equations in the base flow and in the perturbation field are shown in figure 14. For perturbations, the normalization is additionally chosen, so that the maximum energy value is 1 and the time is normalized to ν/u_τ^2 . With such a normalization, the maximum of $P_l + T_l - D_l$ for $Re_\tau = 391$ is $2\lambda_1^+ \approx 0.046$, which agrees with the data presented in figure 14(b). The profile of the energy production in the perturbation field qualitatively coincides with that in the base flow. The maximum production occurs at $y^+ = 16$ (in the base flow at $y^+ = 12$). The energy is transported from the region of maximum production towards the wall to the greatest extent by means of viscous diffusion. It is interesting that the viscous dissipation in the perturbation field is maximal not on the wall, as in the base flow, but in the region of maximum energy production.

Production of the kinetic energy in the base flow is described by the expression $P = -\overline{uv} dU/dy$, where $U(y) = \bar{u}$ is the mean velocity. The expression for the perturbation energy production can be written as follows:

$$\begin{aligned}
 P_l = & \underbrace{-\overline{(\hat{u}_l)^2} \frac{\partial u}{\partial x}}_{P_{11}} - \underbrace{\hat{u}_l \hat{v}_l \left(\frac{\partial u}{\partial y} + \frac{\partial v}{\partial x} \right)}_{P_{12}} - \underbrace{\hat{u}_l \hat{w}_l \left(\frac{\partial u}{\partial z} + \frac{\partial w}{\partial x} \right)}_{P_{13}} \\
 & \underbrace{-\overline{(\hat{v}_l)^2} \frac{\partial v}{\partial y}}_{P_{22}} - \underbrace{\hat{v}_l \hat{w}_l \left(\frac{\partial v}{\partial z} + \frac{\partial w}{\partial y} \right)}_{P_{23}} - \underbrace{\overline{(\hat{w}_l)^2} \frac{\partial w}{\partial z}}_{P_{33}}. \quad (4.6)
 \end{aligned}$$

Figure 15 depicts the distribution of each of the summands of (4.6) showing the role of various mechanisms in the perturbation energy production. Predictably, the maximum contribution of 37% gives the P_{12} term, which can be attributed to the production of perturbation energy by the mean velocity gradient dU/dy . The P_{13} term gives the second largest contribution (21%), which can be attributed to the production of energy in the mixing layers in the lateral direction. The maximum value of P_{13} is reached in the region of the greatest amplitude of velocity fluctuations, $y^+ \approx 15$, while

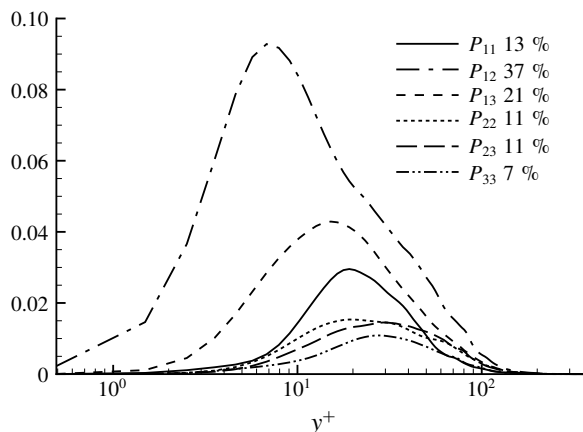


FIGURE 15. $Re_\tau = 391$. Kinetic energy production in perturbation field in the linear stage of development. The profiles of the terms of (4.6) and their percentage contribution into the total perturbation energy production.

the maximum P_{12} is reached closer to the wall at $y^+ \approx 7$. The next contributor is P_{11} with 13%. A significant value of P_{11} reveals the importance of a new mechanism of perturbation production that manifests itself in the slowing-down regions ($\partial u / \partial x < 0$) of the longitudinal velocity of the base flow. Interestingly, all the terms in (4.6) give a positive contribution for each y .

According to the accepted viewpoint, pulsations in a near-wall turbulent flow are produced as a result of the instability of large-scale streaky motion. The dominance of the P_{12} and P_{13} terms in the perturbation energy production reveals that the mean and lateral shear in the base flow are the important factors of perturbation growth. Nonetheless, the noticeable contribution of the other terms indicates that variability of the base flow in the x direction and the presence of motion in the transverse plane can also be significant factors. To verify these assumptions, we investigated evolution of small perturbations on the background of the velocity field of simulation case R391s with the artificially removed short-wave component. In this experiment the behaviour of the perturbation was determined from the solution of the linear equations

$$\frac{\partial \mathbf{u}_l}{\partial t} + (\mathbf{u}_l \nabla) \tilde{\mathbf{u}} + (\tilde{\mathbf{u}} \nabla) \mathbf{u}_l = -\frac{1}{\rho} \nabla p_l + \nu \nabla^2 \mathbf{u}_l, \quad \nabla \mathbf{u}_l = 0, \quad (4.7)$$

where

$$\tilde{\mathbf{u}}(t, y, z) = \langle \mathbf{u} \rangle_x. \quad (4.8)$$

In R391s case, the length of the computational domain is chosen so small that averaging over x will, hopefully, only filter short waves from the base flow that do not seriously affect the properties of its stability. However, the results of the calculations do not support this: the rate of growth of the perturbation actually decreases by more than five times to $\lambda_1^+ \approx 0.004$ (line 2 in figure 16). Note that the velocity field $\tilde{\mathbf{u}}$ in (4.8) contains all three components. If, in the test base flow, only the longitudinal component is retained, and the transversal motion is removed, then

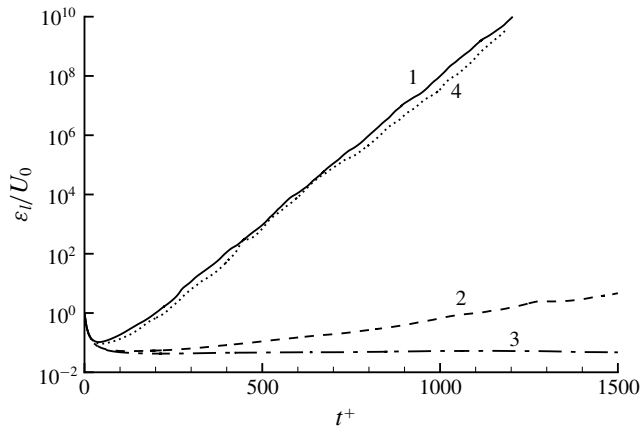


FIGURE 16. Development of perturbations in short simulation domain (simulation R391s). Linear evolution of the perturbation amplitude on the background of the original \mathbf{u} and modified $\tilde{\mathbf{u}}$ velocity fields of the base flow: 1, original base flow, $\lambda_1^+ \approx 0.023$; 2, $\tilde{\mathbf{u}} = (\langle u \rangle_x, \langle v \rangle_x, \langle w \rangle_x)$, $\lambda_1^+ \approx 0.004$; 3, $\tilde{\mathbf{u}} = (\langle u \rangle_x, 0, 0)$, $\lambda_1^+ \approx 0$; 4, $\tilde{\mathbf{u}} = (u - \langle u \rangle_x + \langle u \rangle_{x,z}, v - \langle v \rangle_x, w - \langle w \rangle_x)$.

the growth of the disturbances disappears altogether (line 3 in figure 16). On the contrary, it turns out that the long-wave component of the base flow does not play an important role in generating perturbations of the leading Lyapunov vector. The line 4 in figure 16 shows the evolution of perturbations against the background of the base flow from which the long-wave component is removed:

$$\tilde{\mathbf{u}}(t, x, y, z) = \{u - \langle u \rangle_x + \langle u \rangle_{x,z}, v - \langle v \rangle_x, w - \langle w \rangle_x\}. \quad (4.9)$$

The removal of long waves from the base flow practically does not affect the character of the evolution of the perturbations.

5. Summary and discussion

This work presents a numerical study of perturbation evolution in a developed turbulent flow in a plane channel at moderately low Reynolds numbers of $Re_\tau \leq 586$. The Navier–Stokes equations for an incompressible fluid were solved by the finite-difference method of Nikitin (2006). The results of calculations coincide with high accuracy with those of Moser *et al.* (1999). The calculated steady-state turbulent flows were then used as the base flows for studying the process of perturbation development against their background.

It is shown that, in agreement with the results of previous studies (Nikitin 2008, 2009), the amplitude of small perturbations after a short initial tuning stage ($t^+ < 50$) goes to the exponential growth mode, which corresponds to the output of the solution on to the leading Lyapunov vector (LLV). Contrary to earlier conclusion about the constancy of the highest Lyapunov exponent $\lambda_1^+ \approx 0.021$, a certain increase in λ_1^+ was observed at the largest Re_τ (up to $\lambda_1^+ \approx 0.026$ at $Re_\tau = 586$).

The growth of the perturbations corresponding to the LLV can be related to the presence of large-scale streaky structures in the near-wall layer of the turbulent flow. This is confirmed by the fact that the highest level of disturbances is attained at a

distance of $y^+ = 10\text{--}20$ from the wall, i.e. in the region of the buffer layer of the base flow, where the greatest level of pulsations is observed and, in particular, streaky structures are most pronounced. However, the generation of perturbations of LLV is not an immediate consequence of the instability of the streamwise-uniform streaks, but is dictated by the non-stationarity and inhomogeneity of the short-wave component of the base flow. Outbursts of perturbations activity occur sporadically in different parts of the flow, where locally suitable conditions for their growth occur. The localized perturbation after appearing in one place grows in size and intensity while carrying by the flow and increases the integral amplitude of the perturbations. The next burst starts from an increased perturbations level, thus providing a general exponential growth.

The analysis is made and the contribution of each of the terms entering into the expression for the production of the kinetic energy of the perturbations is determined. The greatest contributions are predictably due to the terms reflecting the generation of perturbations by the mean velocity gradient dU/dy , as well as in the shear layers in the lateral direction. However, the remaining terms reflecting the effects of longitudinal inhomogeneity and the presence of transverse motion in the base flow also make a significant contribution to the generation of perturbations. Neglecting of these effects leads to a significant underestimation of the rate of growth of perturbations.

Based on the form of two-dimensional power spectra in the plane of wavenumbers k_x, k_z the characteristic linear scales were defined and calculated. In general, the results obtained indicate that the structures of the LLV are twice narrower and twice shorter than the structures in the base flow.

We note that the studies carried out in this paper do not give an answer to the question of the existence and the number of other positive Lyapunov exponents in a turbulent flow in a plane channel. Investigation of turbulent flows from the position of dynamics of chaotic systems is not an established approach. The connection between the growing Lyapunov vectors and the structures in turbulent flows has yet to be established. In this connection, it is appropriate to mention the work of Egolf *et al.* (2000), in which Lyapunov exponents were calculated and the properties of Lyapunov vectors in Rayleigh–Bénard convection were studied. It was found that the Lyapunov vectors corresponding to positive exponents are extremely localized both in space and in time. On the contrary, the Lyapunov vectors corresponding to negative exponents are more evenly distributed in space. The results of present paper, relating to the spatio-temporal localization of the LLV structures, agree with the conclusions of Egolf *et al.* (2000). The structures localized in space and time are also observed in near-wall turbulent flows. We note in this connection the so-called turbulent–turbulent spots arising in the near-wall region of the developed boundary layer on a flat plate (Wu *et al.* 2017). It is interesting that the near-wall streaks occur to be inactive in relation to these structures. In this respect, the LLV perturbations considered in the present paper are analogous to the turbulent–turbulent spots found in Wu *et al.* (2017).

Acknowledgements

The author is grateful to Professor A. Yakhot for his helpful comments on a draft of this manuscript. The work was supported by the Russian Foundation for Basic Research under the grant 17-01-00140-a. The research was carried out using the equipment of the shared research facilities of HPC computing resources at Lomonosov Moscow State University.

REFERENCES

- BROOKE, J. W. & HANRATTY, T. J. 1993 Origin of turbulence producing eddies in a channel flow. *Phys. Fluids A* **5**, 1011–1021.
- BUTLER, K. M. & FARRELL, B. F. 1992 Three-dimensional optimal disturbances in viscous shear flow. *Phys. Fluids A* **4**, 1637–1650.
- BUTLER, K. M. & FARRELL, B. F. 1993 Optimal perturbations and streak spacing in wall-bounded turbulent shear flows. *Phys. Fluids A* **5**, 774–777.
- CHERNYSHENKO, S. I. & BAIG, M. F. 2005 The mechanism of streak formation in near-wall turbulence. *J. Fluid Mech.* **544**, 99–131.
- DEL ÁLAMO, J. C. & JIMÉNEZ, J. 2006 Linear energy amplification in turbulent channels. *J. Fluid Mech.* **559**, 205–213.
- DURBIN, P. & WU, X. 2007 Transition beneath vortical disturbances. *Annu. Rev. Fluid Mech.* **39**, 107–128.
- EGOLF, D. A., MELNIKOV, I. V., PESCH, W. & ECKE, R. E. 2000 Mechanisms of extensive spatiotemporal chaos in Rayleigh–Bénard convection. *Nature* **404**, 733–736.
- FARANO, M., CHERUBINI, S., ROBINET, J.-C. & DE PALMA, P. 2017 Optimal bursts in turbulent channel flow. *J. Fluid Mech.* **817**, 35–60.
- FARRELL, B. F. & IOANNOU, P. J. 1996 Generalized stability. Part II. Non-autonomous operators. *J. Atmos. Sci.* **53**, 2041–2053.
- FARRELL, B. F. & IOANNOU, P. J. 2012 Dynamics of streamwise rolls and streaks in turbulent wall-bounded shear flow. *J. Fluid Mech.* **708**, 149–196.
- FARRELL, B. F., IOANNOU, P. J., JIMÉNEZ, J., CONSTANTINO, N. C., LOZANO-DURÁN, A. & NIKOLAIDIS, M.-A. 2016 A statistical state dynamics-based study of the structure and mechanism of large-scale motions in plane Poiseuille flow. *J. Fluid Mech.* **809**, 290–315.
- GINELLI, F., POGGI, P., TURCHI, A., CHATE, H., LIVI, R. & POLITI, A. 2007 Characterizing dynamics with covariant Lyapunov vectors. *Phys. Rev. Lett.* **99**, 130601.
- HAMILTON, K., KIM, J. & WALEFFE, F. 1995 Regeneration mechanisms of near-wall turbulence structures. *J. Fluid Mech.* **287**, 317–348.
- HUTCHINS, N. & MARUSIC, I. 2007 Evidence of very long meandering features in the logarithmic region of turbulent boundary layers. *J. Fluid Mech.* **579**, 1–28.
- INUBUSHI, M., TAKEHIRO, S.-I. & YAMADA, M. 2015 Regeneration cycle and the covariant Lyapunov vectors in a minimal wall turbulence. *Phys. Rev. E* **92**, 023022.
- JANG, P. S., BENNEY, D. J. & GRAN, R. L. 1986 On the origin of streamwise vortices in a turbulent boundary layer. *J. Fluid Mech.* **169**, 109–123.
- JAYARAMAN, A., SCHEEL, J. D., GREENSIDE, H. S. & FISCHER, P. F. 2006 Characterization of the domain chaos convection state by the largest Lyapunov exponent. *Phys. Rev. E* **74**, 016209.
- JEONG, J. & HUSSAIN, F. 1995 On the identification of a vortex. *J. Fluid Mech.* **285**, 69–94.
- JEONG, J., HUSSAIN, F., SCHOPPA, W. & KIM, J. 1997 Coherent structures near the wall in a turbulent channel flow. *J. Fluid Mech.* **332**, 185–214.
- JIMENEZ, J. & PINELLI, A. 1999 The autonomous cycle of near wall turbulence. *J. Fluid Mech.* **389**, 335–359.
- KAWAHARA, G., JIMÉNEZ, J., UHLMANN, M. & PINELLI, A. 1998 The instability of streaks in near-wall turbulence. *CTR Annu. Res. Briefs, Stanford University*, pp. 155–170.
- KEEFE, L., MOIN, P. & KIM, J. 1992 The dimension of attractors underlying periodic turbulent Poiseuille flow. *J. Fluid Mech.* **242**, 1–29.
- KIM, J. & HUSSAIN, F. 1993 Propagation velocity of perturbations in turbulent channel flow. *Phys. Fluids A* **5**, 695–706.
- KIM, H. T., KLINE, S. J. & REYNOLDS, W. C. 1971 The production of turbulence near a smooth wall in a turbulent boundary layers. *J. Fluid Mech.* **50**, 133–160.
- KLEBANOFF, P. S., TIDSTROM, K. D. & SARGENT, L. M. 1962 The three-dimensional nature of boundary-layer instability. *J. Fluid Mech.* **12**, 1–34.
- KLINE, S. J., REYNOLDS, W. C., SCHRAUB, F. A. & RUNSTADLER, P. W. 1967 The structure of turbulent boundary layers. *J. Fluid Mech.* **30**, 741–773.

- LANDAHL, M. T. 1980 A note on an algebraic instability of inviscid parallel shear flows. *J. Fluid Mech.* **98**, 243–251.
- MATSUBARA, M. & ALFREDSSON, P. 2001 Disturbance growth in boundary layers subjected to free-stream turbulence. *J. Fluid Mech.* **430**, 149–168.
- MOSER, R. D., KIM, J. & MANSOUR, N. N. 1999 Direct numerical simulation of turbulent channel flow up to $Re_\tau = 590$. *Phys. Fluids* **11** (4), 943–945.
- NIKITIN, N. 2006 Finite-difference method for incompressible Navier–Stokes equations in arbitrary orthogonal curvilinear coordinates. *J. Comput. Phys.* **217**, 759–781.
- NIKITIN, N. 2007 Spatial periodicity of spatially evolving turbulent flow caused by inflow boundary condition. *Phys. Fluids* **19** (9), 091703-4.
- NIKITIN, N. 2008 On the rate of spatial predictability in near-wall turbulence. *J. Fluid Mech.* **614**, 495–507.
- NIKITIN, N. V. 2009 Disturbance growth rate in turbulent wall flows. *Fluid Dyn.* **44** (5), 652–657.
- NIKITIN, N. V. & CHERNYSHENKO, S. I. 1997 On the nature of the organized structures in turbulent near-wall flows. *Fluid Dyn.* **32**, 18–23.
- NIKITIN, N. V. & PIVOVAROV, D. E. 2018 On the rate of disturbance growth in turbulent Couette flow. *Fluid Dyn.* (submitted).
- PARKER, T. S. & CHUA, L. O. 1989 *Practical Numerical Algorithms for Chaotic Systems*. Springer.
- REDDY, S. C. & HENNINGSON, D. S. 1993 Energy growth in viscous shear flows. *J. Fluid Mech.* **252**, 209–238.
- SCHMID, P. J. & HENNINGSON, D. S. 2001 *Stability and Transition in Shear Flows*. Springer.
- SCHOPPA, W. & HUSSAIN, F. 1997 Genesis and dynamics of coherent structures in near-wall turbulence: a new look. In *Self-Sustaining Mechanisms of Wall Turbulence* (ed. R. Panton), pp. 385–422. Computational Mechanics Publications.
- SCHOPPA, W. & HUSSAIN, F. 1998 Formation of near-wall streamwise vortices by streak instability. *AIAA Paper* 98-3000.
- SCHOPPA, W. & HUSSAIN, F. 2002 Coherent structure generation in near-wall turbulence. *J. Fluid Mech.* **453**, 57–108.
- SMITH, C. R. & METZLER, S. P. 1983 The characteristics of low-speed streaks in the near-wall region of a turbulent boundary layer. *J. Fluid Mech.* **129**, 27–54.
- SREENIVASAN, K. R. 1988 A unified view of the origin and morphology of the turbulent boundary layer structure. In *Proceedings of the IUTAM Symposium on Turbulence Management and Relaminarisation* (ed. H. W. Liepmann & R. Narasimha), pp. 37–61. Springer.
- SWEARINGEN, J. D. & BLACKWELDER, R. F. 1987 The growth and breakdown of streamwise vortices in the presence of a wall. *J. Fluid Mech.* **182**, 255–290.
- TENNEKES, H. & LUMLEY, J. L. 1972 *A First Course in Turbulence*. p. 300. MIT Press.
- TREFETHEN, L. N., TREFETHEN, A. E., REDDY, S. C. & DRISCOLL, T. A. 1993 Hydrodynamic stability without eigenvalues. *Science* **261**, 578–584.
- UNNIKRISHNAN, S. & GAITONDE, D. V. 2016 A high-fidelity method to analyze perturbation evolution in turbulent flows. *J. Comput. Phys.* **310**, 45–62.
- WALEFFE, F. 1995 Hydrodynamic stability and turbulence: beyond transients to a self-sustaining process. *Stud. Appl. Maths* **95**, 319–343.
- WALEFFE, F. 1997 On a self-sustaining process in shear flows. *Phys. Fluids* **9**, 883–900.
- WALEFFE, F. 2003 Homotopy of exact coherent structures in plane shear flows. *Phys. Fluids* **6**, 1517–1534.
- WALEFFE, F. & KIM, J. 1997 How streamwise rolls and streaks self-sustain in a shear flow. In *Self-Sustaining Mechanisms of Wall Turbulence* (ed. R. Panton), pp. 309–332. Computational Mechanics Publications.
- WALEFFE, F., KIM, J. & HAMILTON, J. 1993 On the origin of streaks in turbulent boundary layers. In *Turbulent Shear Flows 8* (ed. F. Durst, R. Friedrich, B. E. Launder, F. W. Schmidt, U. Schumann & J. Whitelaw), pp. 37–49. Springer.
- WESTIN, K. J. A., BOIKO, A. V., KLINGMANN, B. G. B., KOZLOV, V. V. & ALFREDSSON, P. H. 1994 Experiments in a boundary layer subjected to freestream turbulence. Part I: Boundary layer structure and receptivity. *J. Fluid Mech.* **281**, 193–218.

- WU, X., MOIN, P., WALLACE, J. M., SKARDA, J., LOZANO-DURAN, A. & HICKEY, J.-P. 2017 Transitional-turbulent spots and turbulent–turbulent spots in boundary layers. *Proc. Natl Acad. Sci. USA* **114** (27), E5292–E5299.
- XU, M. & PAUL, M. R. 2016 Covariant Lyapunov vectors of chaotic Rayleigh–Bénard convection. *Phys. Rev. E* **93**, 062208.
- ZAKI, T. A. 2013 From streaks to spots and on to turbulence: exploring the dynamics of boundary layer transition. *Flow Turbul. Combust.* **91**, 451–473.